ADVANCED MATERIALS
www.advmat.de

Precisely Tunable Instantaneous Carbon Rearrangement Enables Low-Working-Potential Hard Carbon Toward Sodium-Ion Batteries with Enhanced Energy Density

Junjie Liu, Yiwei You, Ling Huang, Qizheng Zheng, Zhefei Sun, Kai Fang, Liyuan Sha, Miao Liu, Xiao Zhan, Jinbao Zhao, Ye-Chuang Han, Qiaobao Zhang, Yanan Chen, Shunqing Wu, and Li Zhang**

As the preferred anode material for sodium-ion batteries, hard carbon (HC) confronts significant obstacles in providing a long and dominant low-voltage plateau to boost the output energy density of full batteries. The critical challenge lies in precisely enhancing the local graphitization degree to minimize Na^+ ad-/chemisorption, while effectively controlling the growth of internal closed nanopores to maximize Na^+ filling. Unfortunately, traditional high-temperature preparation methods struggle to achieve both objectives simultaneously. Herein, a transient sintering-involved kinetically-controlled synthesis strategy is proposed that enables the creation of metastable HCs with precisely tunable carbon phases and low discharge/charge voltage plateaus. By optimizing the temperature and width of thermal pulses, the high-throughput screened HCs are characterized by short-range ordered graphitic micro-domains that possess accurate crystallite width and height, as well as appropriately-sized closed nanopores. This advancement realizes HC anodes with significantly prolonged low-voltage plateaus below 0.1 V, with the best sample exhibiting a high plateau capacity of up to 325 mAh g^{-1}. The energy density of the HC||$Na_3V_2(PO_4)_3$ full battery can therefore be increased by 20.7%. Machine learning study explicitly unveils the "carbon phase evolution—electrochemistry" relationship. This work promises disruptive changes to the synthesis, optimization, and commercialization of HC anodes for high-energy-density sodium-ion batteries.

1. Introduction

Sodium-ion batteries (SIBs) are emerging as the most promising alternative to lithium-ion batteries (LIBs) in large-scale energy storage and low-speed electric vehicles owing to their low cost,[1] abundant resource reserves, and low-temperature applicability.[2–8] Currently, SIBs are still in the exploration stage of active material screening and battery system optimization.[9–13] In terms of anode materials, hard carbon (HC) has risen above its competitors as the preferred choice for SIBs owing to its comprehensive performance advantages.[14–17]

Structurally, HC is a highly complex carbon alloy composed of randomly-oriented pseudo-graphitic micro-domains, amorphous regions, and open/closed nanopores.[18,19] The structural complexity inevitably determines the diversity of sodium ion storage forms in HC anodes.[20] Despite ongoing debates,[21–24] there is a general consensus that the sodium storage in HC basically follows the

J. Liu, L. Huang, Q. Zheng, K. Fang, L. Sha, M. Liu, X. Zhan, J. Zhao, Y.-C. Han, L. Zhang
College of Chemistry and Chemical Engineering
State Key Laboratory of Physical Chemistry of Solid Surfaces
Tan Kah Kee Innovation Laboratory
Collaborative Innovation Center of Chemistry for Energy Materials (*i*ChEM)
Xiamen University
Xiamen, Fujian 361005, P. R. China
E-mail: zhangli81@xmu.edu.cn

The ORCID identification number(s) for the author(s) of this article can be found under https://doi.org/10.1002/adma.202407369

DOI: 10.1002/adma.202407369

Y. You, S. Wu
Department of Physics
OSED
Key Laboratory of Low Dimensional Condensed Matter Physics (Department of Education of Fujian Province)
Xiamen University
Xiamen 361005, P. R. China
E-mail: wsq@xmu.edu.cn

Z. Sun, Q. Zhang
College of Materials
Xiamen University
Xiamen, Fujian 361005, P. R. China

Y. Chen
School of Materials Science and Engineering
Key Laboratory of Advanced Ceramics and Machining Technology (Ministry of Education)
Tianjin University
Tianjin 300072, P. R. China

"adsorption-filling" mechanism.[25,26] On one hand, the ad-/chemisorption of Na^+ ions at defect sites and open surfaces gives rise to a slope region in the high-voltage interval between 1.0 and 0.1 V, and normally accounts for more than 30% of the overall capacity.[27,28] On the other hand, the filling of Na^+ ions into closed nanopores in a quasi-metallic state brings about a low-voltage plateau region below 0.1 V.[29–32] Notably, HC shows a strong precursor dependence on its carbon microstructures and heteroatoms.[23,33,34] This essentially leads to significant differences in slope region and plateau region capacities of HCs obtained from diverse biomass feedstocks.[34,35]

From the perspective of full batteries, people prefer HCs to offer long and dominant low-voltage discharge/charge plateaus like the graphite anode in LIBs.[36–38] This is because the high-voltage slope region of HC is detrimental to both the output cell voltage and energy density of SIB full batteries.[39,40] This raises a very important scientific question: how to maximize plateau capacity below 0.1 V and minimize slope region capacity by precisely modulating the various carbon phases (including crystalline carbon, amorphous carbon, and nanopores) in HCs?

High-temperature sintering is the most direct and universal approach for regulating the microstructures of carbonaceous materials.[41] When subjected to elevated temperatures, the pseudo-graphitic micro-domains in HCs become more long-range ordered, while the proportion of amorphous carbon decreases, accompanied by a reduction in defect levels.[22] Apparently, this is highly beneficial in reducing the Na^+ ad-/chemisorption at defect sites and diminishing the slope region capacity. However, high-temperature treatment is a "double-edged sword" for HCs, that is, when the slope region capacity decays to a certain threshold, the plateau capacity, and the overall capacity will decline sharply accordingly. This is because the carbon phase transition from amorphous to crystalline will promote the closed pore growth inside the HCs. With the increase in pore size, the nanopores will gradually become partially available or even unfillable for Na^+ ions owing to a combination of factors such as weakened induced nucleation activity, limited Na^+ conductivity of high-crystallinity graphene walls, as well as low thermodynamic probability of larger quasi-metallic cluster formation.[42–45] Therefore, the current heat treatment of HCs has to find a trade-off between crystallinity and pore structure at moderate temperatures (1400–1500 °C), which is manifested in commercial HCs retaining considerable slope region capacity to avoid severe plateau capacity loss.[46]

Very recently, a few special precursors containing easy graphitizable components, for example, charcoal,[47] bamboo,[48] and wood rich in crystalline cellulose,[49] have been screened out and broke through the inherent contradiction between graphitization and pore growth of HCs, resulting in the plateau region-dominated HC anodes. Impressively, Chou et al. achieved all-plateau and high-capacity topological graphitized carbon by utilizing corn cobs as the precursor.[50] Although these isolated cases are highly precursor dependent, they all indicate that easily graphitized components can form locally highly graphitized regions at lower temperatures, thus guaranteeing the formation of usable nanopores of appropriate size.

To fundamentally solve the mutual constraint between graphitization degree enhancement and nanopore growth, and get rid of the dependence on precursors, here we have designed and introduced modified flash Joule heating technology in the preparation of metastable HC anodes for the first time, transforming the modulation of carbon phases inside HCs from a thermodynamically controlled process to a kinetically controlled process.[51–54] By precisely controlling the temperature and width of transient thermal pulses, we can accurately regulate the local graphitization degree and closed pore growth of HCs within seconds, obtaining HCs with both short-range ordered graphitic micro-domains and appropriately sized closed nanopores (**Figure 1a,b**). More encouragingly, these kinetically controlled HC products can well persist over long periods and show a significantly prolonged low-working-voltage plateaus below 0.1 V, with the best sample exhibiting a high plateau capacity of up to 325 mAh g^{-1} (89.5% of overall capacity, Figure 1c), which is at the forefront of current research in whole-plateau hard carbon. Most importantly, this high-plateau-capacity HC enables us to construct HC || $Na_3V_2(PO_4)_3$ full batteries with an energy density increment of up to 20.7%. This technique is universally applicable and precursor-independent, allowing for the precise regulation of both commercialized and independently synthesized HCs. We experimentally and theoretically elucidate the structural evolution of carbon phases and closed nanopores under pulses of different widths, as well as their correlation with sodium storage electrochemistry. Our work provides transformative solutions for the structural optimization and performance breakthrough of various carbonaceous electrode materials in the field of sustainable energy storage/conversion devices.

2. Results and Discussion

2.1. Correlation Between Precisely Tunable Carbon Phases and Sodium Storage Electrochemistry

Utilizing a self-built Joule heating setup equipped with circulating cooling (Figure S1, Supporting Information), we subjected commercial HC materials (BTR New Materials Group Co. Ltd.) to a 1550 °C thermal pulse while precisely controlling the pulse widths to be 5, 10, 20, 30, 45 and 60 s, respectively. The obtained samples are defined as HC (x s), where x represents the thermal pulse widths. Notably, the upper limit temperature for processing conventional biomass HCs is usually below 1500 °C, and heat treatment exceeding this temperature often leads to a significant decay in plateau capacity, primarily due to the fact the larger-sized nanopores formed at higher temperatures can only be partially filled with Na^+ or even unfillable at all. **Figure 2a** for the first time discloses the drastic changes in the sodium storage electrochemistry of HC anodes after being treated with various pulse widths at the same temperature. As the pulse width increases, the voltage of the slope region in the discharge curves of HC anodes shows a continuous downward trend, while the voltage of the slope region in the charge curves is also continuously decreasing. Influenced by this, the average working voltages during the discharge and charge processes of HC anodes show a continuous decreasing trend (Figure S2, Supporting Information). Specifically, the total capacity shows a trend of first increasing and then decreasing. There are maximum values of reversible charge capacity and plateau capacity at thermal pulse widths of 20 and 30 seconds, respectively (Figure 2a). To further

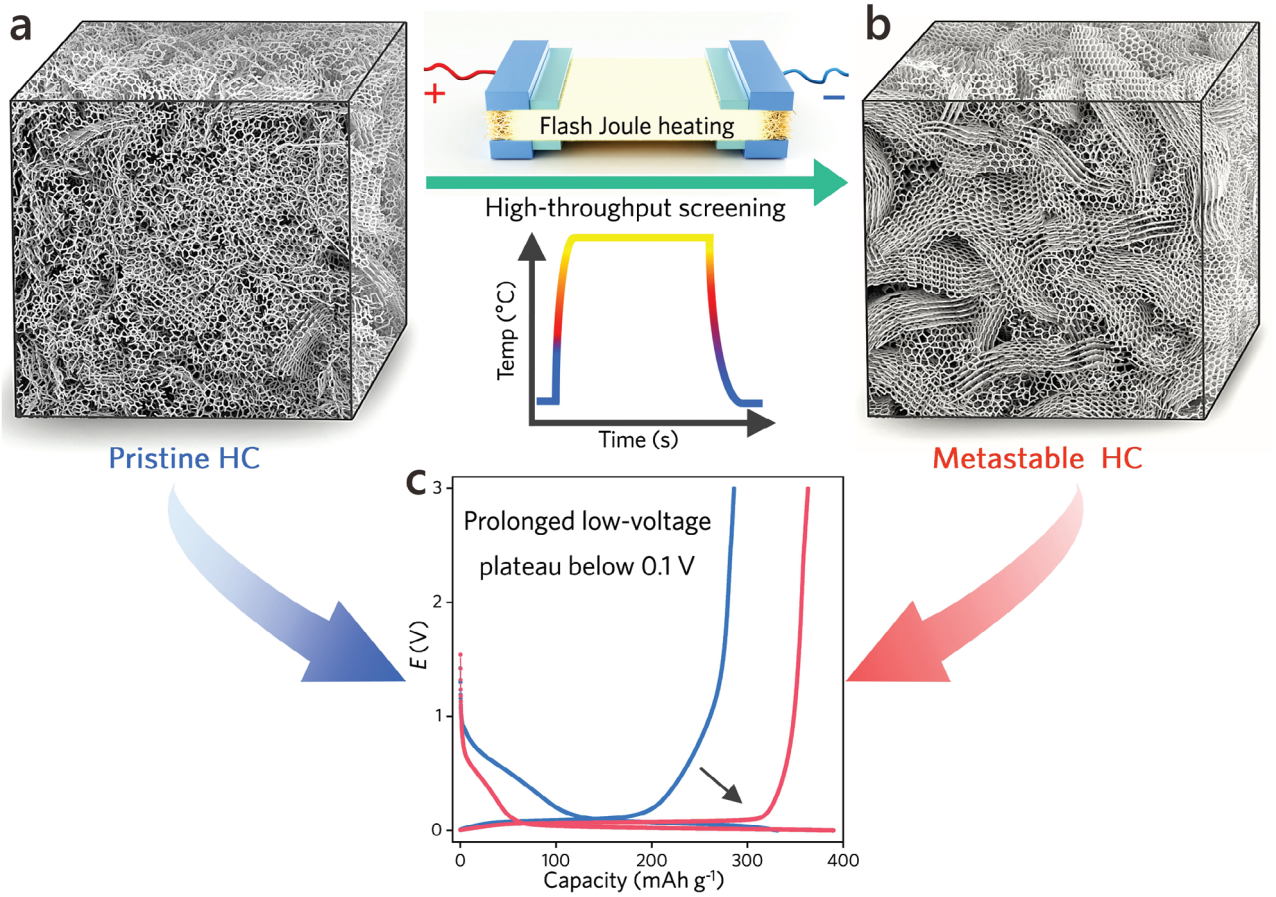

Figure 1. Schematic diagram of synthesizing HCs with precisely tunable carbon phases and low working potential plateaus. a) Schematic of carbon phases, including crystalline carbon, amorphous carbon, and nanopores, in the pristine HC. b) Schematic of carbon phases in the metastable HC after modified flash Joule heating. c) Precise carbon phase modulation endows HCs with significantly prolonged and dominant low-voltage plateaus below 0.1 V.

quantitatively analyze the variations in plateau capacity and total capacity with thermal pulse width, we define the part of the discharge curve below 0.1 V and the part of the charge curve below 0.2 V as the plateau region, while the remaining parts are classified as the slope region for subsequent discussions. As manifested in Figure 2b,c, both the plateau capacity during discharge and charge processes reached an identical maximum value of 255 mAh g^{-1} after a flash sintering of 30 s, significantly outperforming those of 204 and 207 mAh g^{-1} for the pristine HC sample (Figure S3, Supporting Information). Notably, both the plateau capacity and total capacity showed a drastic decay after a thermal pulse exceeding 30 s, indicating that the modulation effect of long thermal pulses on the carbon microstructures tends to be consistent with traditional thermal treatment. Moreover, the slope region capacity continues to decrease as the pulse width increases in both the discharging and charging processes (Figure S4, Supporting Information), which is consistent with what we found in Figure 2a. Interestingly, after flash sintering for 30 s or longer, the ratio between slope region capacity and plateau capacity remains basically unchanged (Figure S5, Supporting Information), possibly implying that the total capacity decay is related to a decrease in the overall material utilization.

To gain insight into microstructural changes in HCs within a 60-second thermal pulse and their correlation with electrochemical performance, we first studied the evolution of local graphitization using Raman, Fourier Transform infrared spectroscopy (FTIR) and X-ray diffraction (XRD) spectroscopy. As disclosed in Figure S6 (Supporting Information), no visible changes can be observed in the FTIR spectra of HCs with increasing thermal pulse width, indicating that the types and compositions of valence bonds remain unchanged. By contrast, Raman spectra reveal abundant information about the evolution of carbon microstructure. As Figure 2d,e demonstrate, the Raman spectra exhibit three characteristic peaks, namely the D band at 1350 cm^{-1}, G band at 1580 cm^{-1} and 2D band at 2700 cm^{-1}, which are assigned to the out-of-plane vibrations of structural defects, in-plane vibrations of sp^2 bonded carbon atoms and the thickness of graphitic carbon.[55,56] As the pulse width increases, the intensity of the G band gradually increases while the intensity of D band continues to decrease. The value of I_G/I_D increases from 0.86 to 1.61, indicating that the degree of local graphitization within HCs is greatly enhanced. Moreover, when the pulse width reaches 20 s or more, a 2D band appears in the spectra with increasing intensity, suggesting that the thickness of graphitic micro-domains is continuously increasing, and this process is clearly presented in the contour map (Figure 2e).

XRD analysis can provide more quantitative average information about the carbon phase evolution. As illustrated in

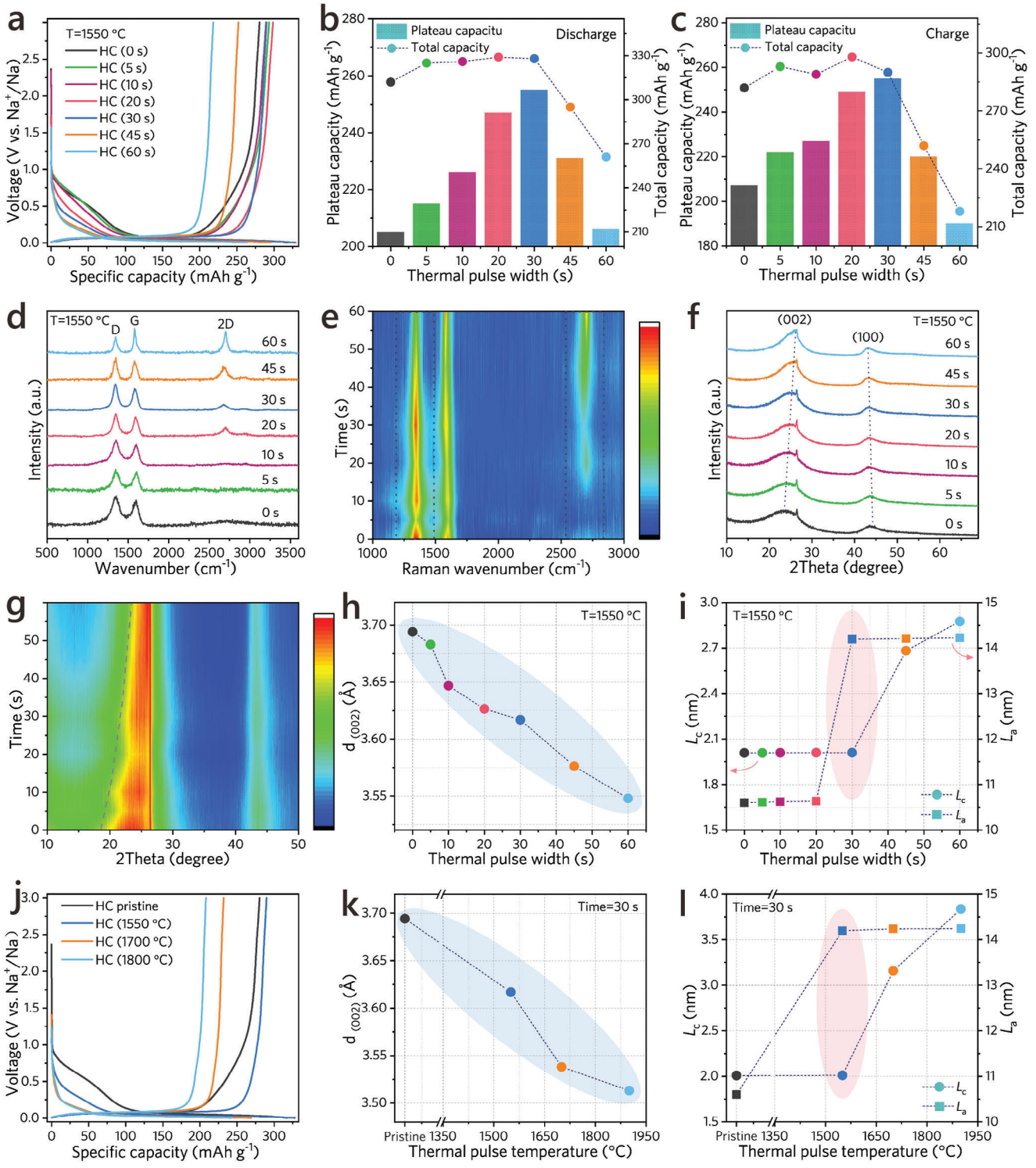

Figure 2. Drastic carbon phase evolution of commercial HCs under different thermal pulse widths and temperatures. a) First-cycle discharge and charge profiles of HC anodes after being treated with different pulse widths at 1550 °C. b,c) Plateau capacities and total capacities of HC anodes after flash sintering for various durations during the discharge and charge processes, respectively. d,e) Raman spectra and corresponding contour maps of HCs after flash sintering for various durations. f,g) XRD spectra and corresponding contour maps of HCs after flash sintering for various durations. h) Measured $d_{(002)}$ (interlayer spacing of amorphous carbon (002) peak) values of HCs after flash sintering for various durations. i) Average crystallite width (L_a) and crystallite height (L_c) of graphitic micro-domains in HCs after flash sintering for various durations. j) First-cycle discharge and charge profiles of HC anodes before and after being treated at 1550, 1700 and 1900 °C with a same pulse width of 30 s. k) Measured $d_{(002)}$ values of HCs before and after flash sintering at 1550, 1700 and 1900 °C for 30 s. l) Average L_a and L_c of graphitic micro-domains in HCs before and after flash sintering at 1550, 1700 and 1900 °C for 30 s.

Figure 2f,g, two broad peaks appear at 23.5° and 43.8° corresponding to (002) and (100) crystal planes of disordered amorphous structure,[30] while a sharp peak at 26.4° is assigned to the (002) plane of inherent graphite component in HC. As the thermal pulse width prolongs, the amorphous carbon peak located at 23.5° gradually shifts toward a higher angle and eventually merges with the (002) graphite peak, indicating a continuous enhancement in the degree of localized graphitization within the HC. The interlayer spacing $d_{(002)}$ of amorphous carbon (002) peak, as well as average crystallite width (L_a) and crystallite height (L_c) of graphitic micro-domains were further calculated by Bragg and Scherrer formulas and presented in Figure 2h,i and Table S1 (Supporting Information). As Figure 2h demonstrates, $d_{(002)}$ of amorphous carbon decreases from 3.694 to 3.548 Å as time progresses, strongly confirming the enhanced degree of localized graphitization. The variations in L_a and L_c reflect more interesting information on the evolution of graphitic micro-domains. As the thermal pulse width increases, L_a starts to increase slowly and undergoes a sudden surge at 30 s, followed by a gradual rise. By contrast, L_c grows slowly in the first 30 s but then maintains a rapid increase. Combined with electrochemical performance (Figure 2a), the maximum value of plateau capacity appears in a narrow time window when L_a undergoes a sudden jump but L_c does not change significantly, that is, the graphitic micro-domains are just in a short-range ordered state with fewer layers.

The impact of different temperatures on the carbon phases and sodium storage electrochemistry of HC anodes is shown in Figure 2j and Figure S7 (Supporting Information). After undergoing the same 30 s, the total capacity and plateau capacity of HCs treated at 1700 and 1900 °C showed significant decreases compared to those treated at 1550 °C. The prominent 2D band in the Raman spectrum indicates a significant increase in the layer numbers of graphitic micro-domains of HC at 1900 °C (Figure S8, Supporting Information). Moreover, the $d_{(002)}$ of amorphous carbon reached 3.538 and 3.513 Å after being treated at 1700 and 1900 °C for 30 s, respectively, revealing a high degree of graphitization (Figure 2k; Figure S9). More interestingly, L_a remains almost unchanged as the temperature rises from 1550 to 1900 °C, while L_c continues to increase (Figure 2l; Table S2, Supporting Information). Combining with electrochemical performance, we can once again confirm that the sharp increase in L_c is the direct cause of the reduction in total capacity and plateau capacity. Note that the rise of L_c can be effectively avoided by adopting shorter thermal pulses under high temperatures, thereby achieving a considerable plateau capacity. For example, reducing the width of the thermal pulse at 1700 °C from 30 to 15 s can result in a plateau capacity as high as 269 mAh g^{-1} (Figure S10, Supporting Information).

2.2. Evolution of Graphitic Micro-Domains and Closed Nanopores Within Short Thermal Pulses

In HCs, the formation and evolution of closed nanopores are highly related to and mutually influenced by the variation of graphitic micro-domains.[57,58] The evolution of local graphitic domains and nanopores is further elucidated in relation to the increasing thermal pulse widths through high-resolution transmission electron microscopy (HRTEM). As **Figures 3a** and S11 (Supporting Information) demonstrate, the degree of graphitization in pristine HCs is very low, and the graphitic micro-domains are composed of twisted and defect-rich graphene ribbons (green boxes, where the length and width correspond to L_a and L_c, respectively). Meanwhile, a small number of closed nanopores (yellow circles) can be observed, which is consistent with the distinct slope region and low plateau capacity of the untreated HC anode (Figure 2a). When the thermal pulse width reaches 10 s, the local graphitization degree of HC (10 s) was significantly improved, and the pore size of closed nanopores was slightly increased (Figure 3b; Figure S12, Supporting Information). More importantly, the defect degree of graphene ribbons constituting graphitic micro-domains was also greatly reduced, resulting in the formation of some open nanopores that have not been closed (yellow dotted circles), which can explain why the plateau capacity after 10 s treatment has markedly enhanced but has not yet reached its maximum value. When the thermal pulse width increases to 30 s (Figure 3c; Figure S13, Supporting Information), the HC (30 s) sample showed dramatically reduced defect level and noticeably increased L_a (green boxes). Due to the topological connection of graphitic micro-domains, the open nanopores inside HC were eventually transformed into closed nanopores of appropriate size. This is highly consistent with the experimental observation that the plateau capacity of the HC (30 s) anode reaches its maximum value (Figure 2a). Note that the apparent morphology of the pristine HC and HC (30 s) has not changed at all, and the chemical information of the sample surface also remains unchanged (Figures S14 and S15, Supporting Information). This implies that the change in internal carbon phase is the fundamental reason for the significant variation in electrochemical properties.

After experiencing a 60 s thermal pulse, the crystallinity and L_c of graphitic micro-domains in HC (60 s) were further promoted, resulting in the formation of larger closed pores (Figure 3d; Figure S16, Supporting Information). Apparently, Na^+ ions will encounter great resistance when penetrating through highly crystallized and thicker graphene walls. Theoretical computations also reveal that Na^+ ions are not likely to nucleate and form stable quasi-metallic clusters within larger closed pores with lower defect density.[39–42] This reasonably elucidates the underlying mechanism behind the drastic decline in total capacity and plateau capacity after 60 s thermal pulse treatment. The negative impact of larger pores with high thickness and low defect level on the plateau and total capacity of HCs was amplified and revealed by using a graphitization furnace to calcinate HC samples at 2800 °C. As Figure S17 (Supporting Information) demonstrates, the HC (2800 °C) sample exhibits extremely high crystallinity and nanopores with more than 15 layers. As expected, these large nanopores are almost unfillable to Na^+ ions, resulting in a very low plateau capacity and overall capacity (Figure S18a, Supporting Information).[42]

Special aberration-corrected TEM further compared the carbon microstructure of the HC (0 s) and HC (30 s) samples at a higher spatial resolution (Figure 3e,f). Apparently, the graphitization degree of the pristine HC is low, and there are a few small-sized closed pores and more unclosed open pores. By contrast, the local graphitization degree of the HC (30 s) sample has

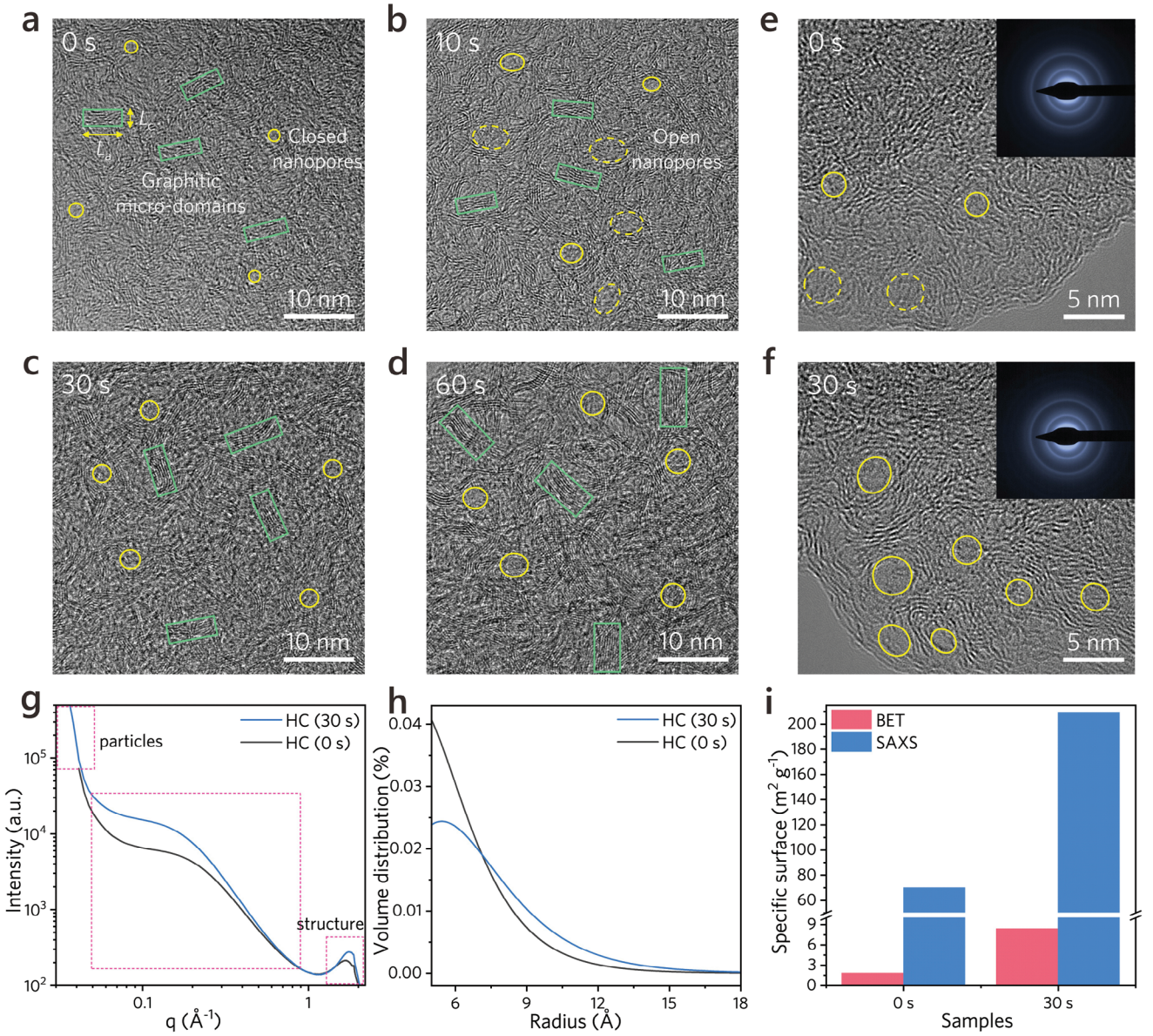

Figure 3. Evolution of graphitic micro-domains and closed nanopores during flash sintering. a–d) HRTEM images of HCs before and after being treated for 10, 30, and 60 s at 1550 °C. e,f) Special aberration-corrected TEM images of pristine HC (0 s) and HC (30 s) samples. g) SAXS scattering curves of HC (0 s) and HC (30 s) samples. h) Pore size distribution curves of HC (0 s) and HC (30 s) samples. i) Bar graph of BET and SAXS-fitted specific surface areas of HC (0 s) and HC (30 s) samples. Note that the specific surface area of closed nanopores was calculated by subtracting the BET area from the SAXS-fitted specific surface area.

been greatly improved, and a large number of closed pores of suitable size are evenly distributed. To quantitatively study the changes brought by transient high-temperature pulses to the HC pore structure, true density measurement and small-angle X-ray scattering (SAXS) (Figures S19 and S20, Supporting Information) were performed.[59,60] As presented in Table S3 (Supporting Information), the true density of HC (0 s) and HC (30 s) were measured to be 2.13 and 1.49 g cm^{-3}, manifesting that the HC shows a richer pore structure after a 30 s thermal pulse. Moreover, the SAXS pattern of HC (30 s) shows a higher intensity in the intermediate q region (Figure 3g), again confirming that the thermal pulse-treated HC possesses more nanopores (including closed and open pores).[33,61] The derived pore size distribution curves indicate that the main pore size of HC (30 s) sample is 11.42 Å, which is larger than that (9.23 Å) of the pristine HC (Figure 3h). The specific surface area of closed nanopores was estimated by subtracting the Brunauer-Emmett-Teller (BET) area (open pores, Figure S21, Supporting Information) from the SAXS-fitted specific surface area (total pores, Figure S19, Supporting Information).[62] Apparently, the main pores in the HC (30 s) sample are closed pores rather than open pores, and the surface area of closed nanopores was significantly increased from 68.14 to 201.2 m^2 g^{-1} after the thermal pulse treatment (Figure 3i; Figure S22, Supporting Information). These quantitative results

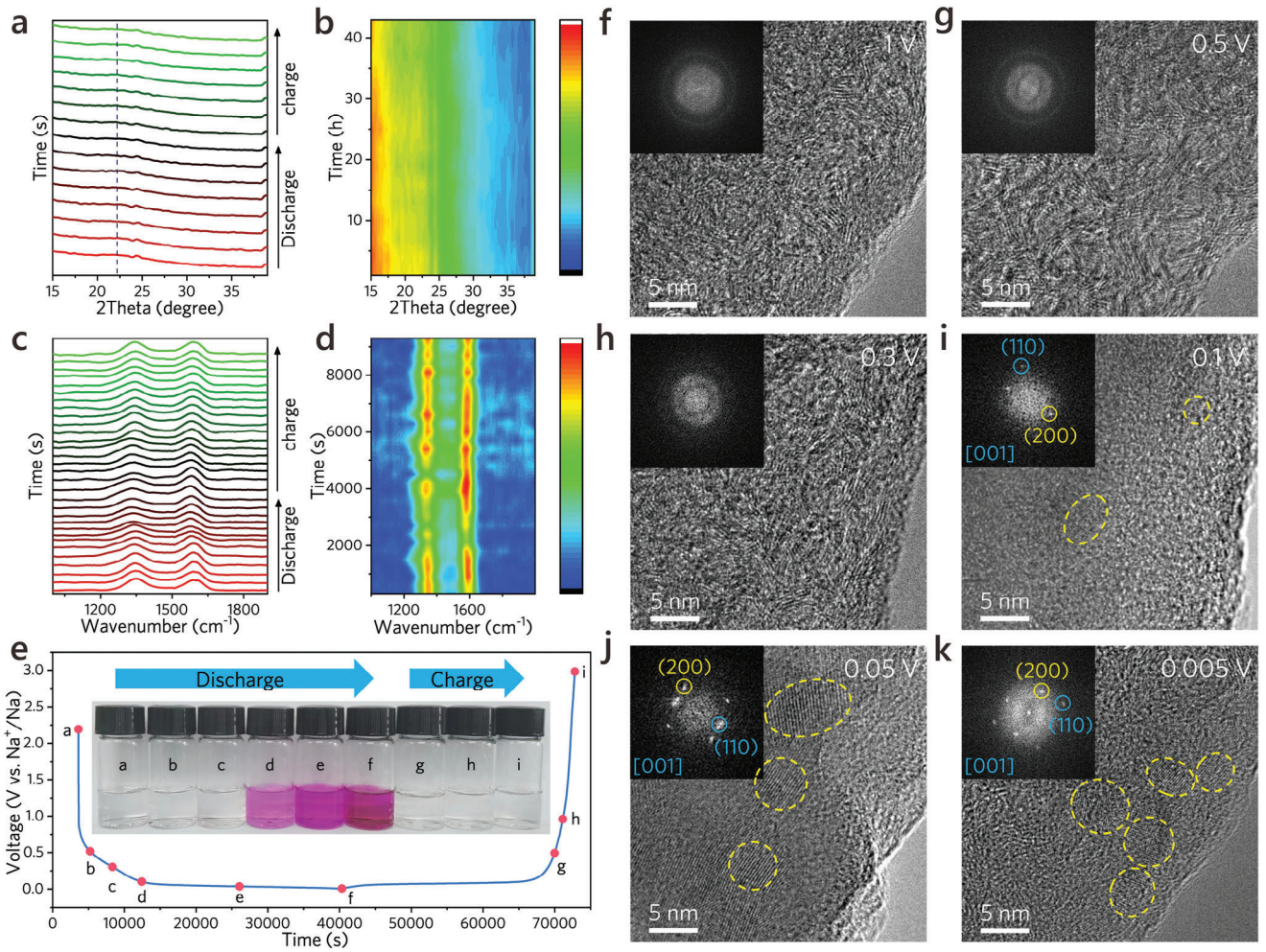

Figure 4. Characterizations of Na^+-ion storage in the HC (30 s) during discharge/charge processes. a,b) in situ XRD spectra and corresponding contour maps of the HC (30 s) anode during discharge/ charge processes. c,d) in situ Raman spectra and corresponding contour maps of the HC (30 s) anode during discharge/charge processes. e) Colorimetry experiment of HC (30 s) electrodes at the OCP and after being discharged to 1, 0.5, 0.3, 0.1, 0.05, 0.005 V and charged to 0.3, 0.5 and 3 V in an ethanol solution containing phenolphthalein. f–k) ex situ HRTEM images of HC (30 s) anodes after discharged to six different potentials of 1, 0.5, 0.3, 0.1, 0.05, and 0.005 V, respectively.

of pore formation and evolution are highly consistent with the observations of TEM.

2.3. Characterizations and Machine-Learning Study of Na^+-Storage Mechanism in Optimal HCs

In order to elucidate the sodium ion storage mechanism in our optimal HC (30 s), in situ XRD, electrochemical impedance, Raman and ex situ TEM characterizations were further performed (**Figure 4**; Figure S23, Supporting Informastion). As Figure 4a,b demonstrate, the (002) peaks in the stacked XRD spectra did not show visible shifts throughout the discharge and charge processes, confirming that no Na-ion intercalation occurred between the graphitic carbon interlayers.[63] In situ Raman provides more information about Na^+ ion adsorption and pore filling.[64] As the potential gradually decreases during discharge, Na^+ ions successively undergo ad-/chemisorption at defect sites and fill in the closed nanopores, resulting in a reduction in defect sites in HCs and a decrease in electron cloud density between graphitic carbon interlayers. These variations lead to a gradual decrease in I_D/I_G and negative shift (blue shift) of G bands in the stacked Raman spectra (Figure 4c,d). In the subsequent charge process, these trends are exactly opposite and highly reversible.

To provide more direct evidence for the filling behavior of Na^+ ions in the closed pores of the optimal HC (30 s), we disassembled the HC anode electrodes at the open circuit potential (OCP), as well as discharged to 1, 0.5, 0.3, 0.1, 0.05, 0.005 V and charged to 0.5, 1.0 and 3 V from the half cells and soaked them in an ethanol solution containing phenolphthalein (Figure 4e).[29] Apparently, the three HC electrodes discharged to 0.1 V or below (i.e., entering the plateau region) have caused the solution to turn red and the color gradually deepens, which convincingly confirms that the low-potential capacity is indeed generated by filling closed nanopores with metallic sodium. More importantly, the electrodes in the charged states no longer turned the solution red, indicating that the metallic sodium has completely returned to the cationic state and the pore-filling process is highly reversible.

To gain a deep understanding of the morphology of metallic sodium formed during the discharge process, we conducted in situ TEM characterization of HC anodes in the initial three cycles (Figure S24, Supporting Information) and ex situ TEM characterization on HC anodes after discharged to six different potentials (Figure 4f–k). As expected, no new phase was formed inside the HC anode after discharged to 0.3 V, indicating that sodium storage in the slope region is dominated by Na^+ ion adsorption. Moreover, metallic sodium clusters with an average particle size of a few nanometers (dotted yellow circles) began to appear when discharged to 0.1 V, and their number increased with the decrease in voltage. By further analyzing the lattice with fast Fourier transform (FFT), in situ TEM showed that lots of lattice streaks appeared at the end of the first discharge (Figure S25, Supporting Information). By using SAXS and ^{23}Na NMR spectroscopy, the filling of sodium clusters in the closed nanopores of hard carbons can also be clearly observed (Figure S25, Supporting Information). Moreover, diffraction points corresponding to the (100) and (200) crystal planes of metallic sodium can be observed after discharged to 0.1 V (inset of Figure 4i), and the signal strengthens with decreasing potential (insets in Figure 4j,k). The above results intuitively illustrate that in the low-voltage plateau region, pore-filling in a metallic state is the dominant storage form for Na^+ ions in our HC materials. Notably, no sodium precipitation phenomenon can be observed on the HC anode surface of the first three cycles and after discharged to 0.005 V (Figures S25 and S26, Supporting Information), revealing that the pore-filling process is fundamentally different from the traditional electrodeposition, which typically occurs at a lower potential of ≈−0.01 V (Figure S27, Supporting Information).

Previous first-principles calculations have shown:[65] that the adsorption energies of Na intercalated in graphite are all positive, indicating that it is difficult for sodium ions to be stored in graphite through intercalation. However, lithium ions can be stored in graphite through intercalation, so the storage mechanisms of Na and Li are different. This is in accord with our observations in the in situ XRD analysis (Figure 4a), and it also demonstrates that the continuous increase in the layer numbers of pseudo-graphitic microdomains is detrimental to Na^+ ion transport and sodium cluster nucleation.

Our experiments show the discharge profile can be divided into two regions: the slope region and the plateau region. To better understand the Na^+ storage mechanisms in these two voltage intervals, we performed a study of the discharge curve using machine learning interatomic potentials (Figures S28–S31, Supporting Information). We constructed an HC model (250000 atoms) to perform molecular dynamics simulations of Na-ion storage, and a schematic of the process is shown in **Figure 5**a. Specifically, the atomistic models of HC were constructed with specific values of L_a and L_c. To introduce diversity, the graphite microdomains with set L_a and L_c are randomly rotated by an arbitrary angle in 3-D space, and this process is repeated multiple times, resulting in numerous graphite sheets with random orientations. Next, we randomly select and assemble these graphite sheets in 3D space, ensuring a compact structure.

Molecular dynamics simulations are conducted on this assembled structure to obtain the target model (Figure 5). Figure 5c presents a hard carbon model where Na^+ ions are fully occupied (i.e., fully discharged). We further divided the voltage profile into three regions (Figure 5b), with the corresponding Na^+ ion insertion sites in each region depicted in Figure 5d–f. During discharging, Na^+ ions first anchor at the edge sites between graphene layers in the graphitic micro-domains. This is followed by further immobilization of Na^+ ions near these sites, or adsorption of Na^+ ions on the surface. The voltages corresponding to these two Na storage sites are relatively high, manifesting as the slope region (I and II in Figure 5b). The plateau region corresponds to the continuous embedding based on the slope region, where the prior Na^+ ion implantation facilitates the subsequent Na-ion storage in the closed pores similar to "house of cards", resulting in a low working potential (III in Figure 5b). More importantly, Na^+ ions stored in the plateau region mostly exist in the form of sodium clusters (yellowish-brown balls), which is in consistence with the observations of ex situ TEM. It is worth emphasizing that, the high alignment between our simulated discharge curve and experimental data (blue curve in Figure 5b) convincingly validates the predictive capability of the atomic-level potential.

We have shown that the thermal pulse widths significantly affect the L_a and L_c values, and further determine the overall capacity and potential plateaus. Here we constructed structural models with different L_a and L_c, and theoretically elucidated the impact of these variables on the sodium storage electrochemistry of HCs. Figure 5g,h show the simulated discharge curves corresponding to different L_a and L_c, respectively. When L_c is fixed and L_a monotonically increases, the slope region capacity shows a continuous downward trend. This is mainly because the higher L_a per unit mass of graphitic micro-domains, the fewer anchoring sites for Na^+ ions. Moreover, the size of L_a does not directly affect the overall capacity of the HC anode, which is consistent with what we found in Figure 2a,i. By contrast, with the increase of L_c, the slope region capacity gradually increases, but the plateau capacity and overall capacity continue to decrease (Figure 5h). This is because the increase in the layer numbers of the graphitic microdomains can provide more edge interlayer sites, thereby boosting the slope region capacity. Meanwhile, since Na^+ ions cannot intercalate into the graphite layers, the more graphene layers per unit mass of graphitic micro-domains, the lower thermodynamic probability of forming quasi-metal clusters, resulting in a simultaneous decrease in plateau and total capacity. The relationship between L_c thickness and capacity from calculations and experiments are both shown in Figure 5i, demonstrating the same trend of change. Both theoretical calculations and experimental results demonstrate that short-range ordered graphitic microdomains, especially those with appropriate L_a and lower L_c, are most beneficial for achieving high plateau and total capacity.

2.4. The HC (30 s) Anode Enhances the Energy Density of Na-Ion Full Batteries by Over 20%

Figure 6a shows the first-cycle discharge/charge profiles of pristine HC and HC (30 s) in half-cells at 30 mA g^{-1}. Apparently, the HC (30 s) anode shows a significantly longer plateau region during both discharge and charge processes, which accords well with what we found in Figure 2a. The HC (0 s) anode delivers discharge and charge capacities of 317.2 and 280.4 mAh g^{-1}, respectively, corresponding to an initial Coulombic efficiency of 88.39%. By contrast, the HC (30 s) anode exhibits higher

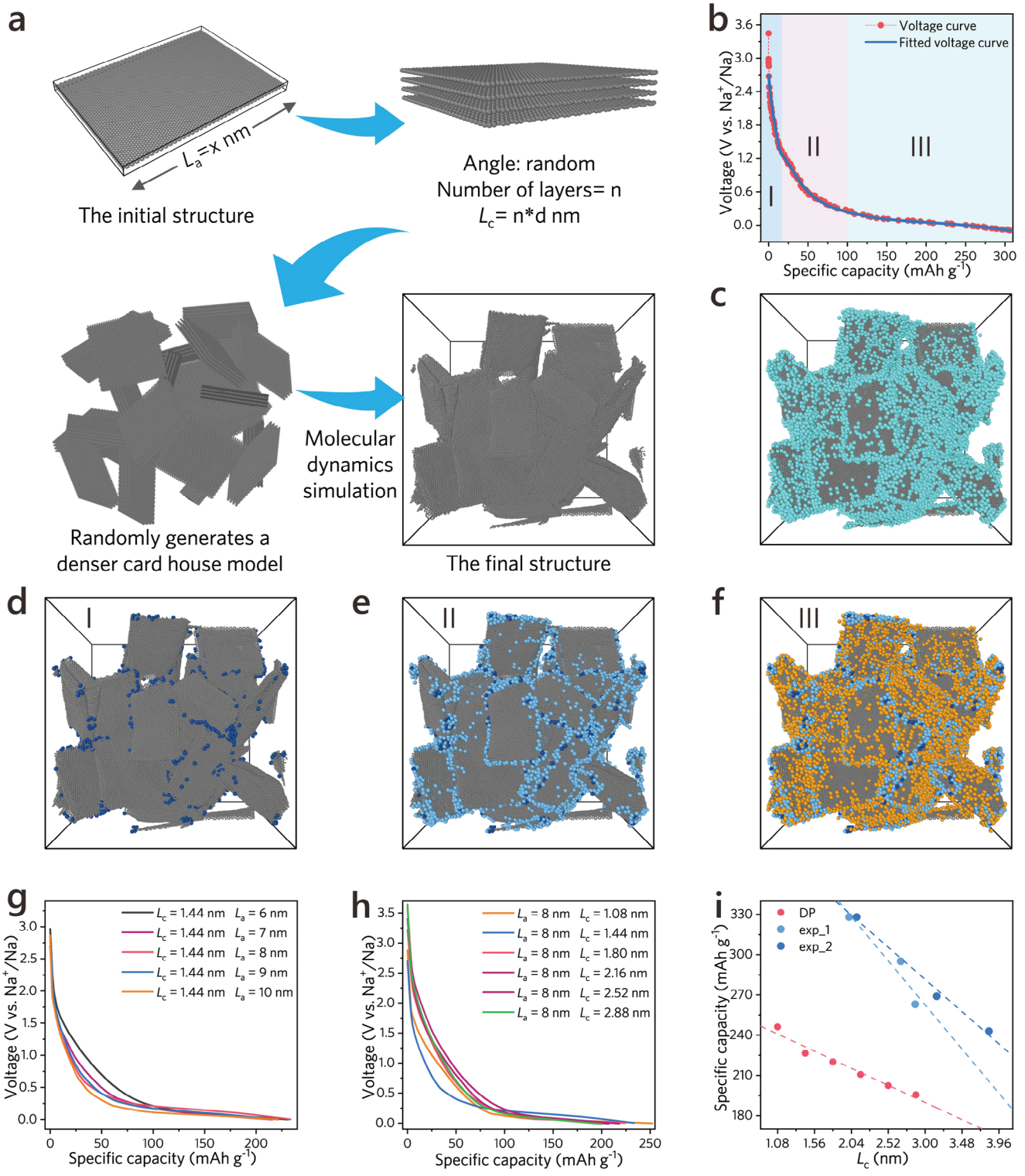

Figure 5. Machine-learning study of Na^+-ion storage mechanism in HCs. a) Schematic diagram of the modeling process. b) The measured and fitted voltage curves of the discharge process. c) The structural model of HC with maximum Na^+ storage in a fully discharged state. d-f) Structural models of HC in three different stages (I, II, and III in 5c) during the discharge process. g) The correlation between voltage profile and specific capacity at fixed L_c value and continuously changing L_a values. h) The correlation between voltage profile and specific capacity at fixed L_a value and continuously changing L_c values. i) The relationship between L_c and specific capacity.

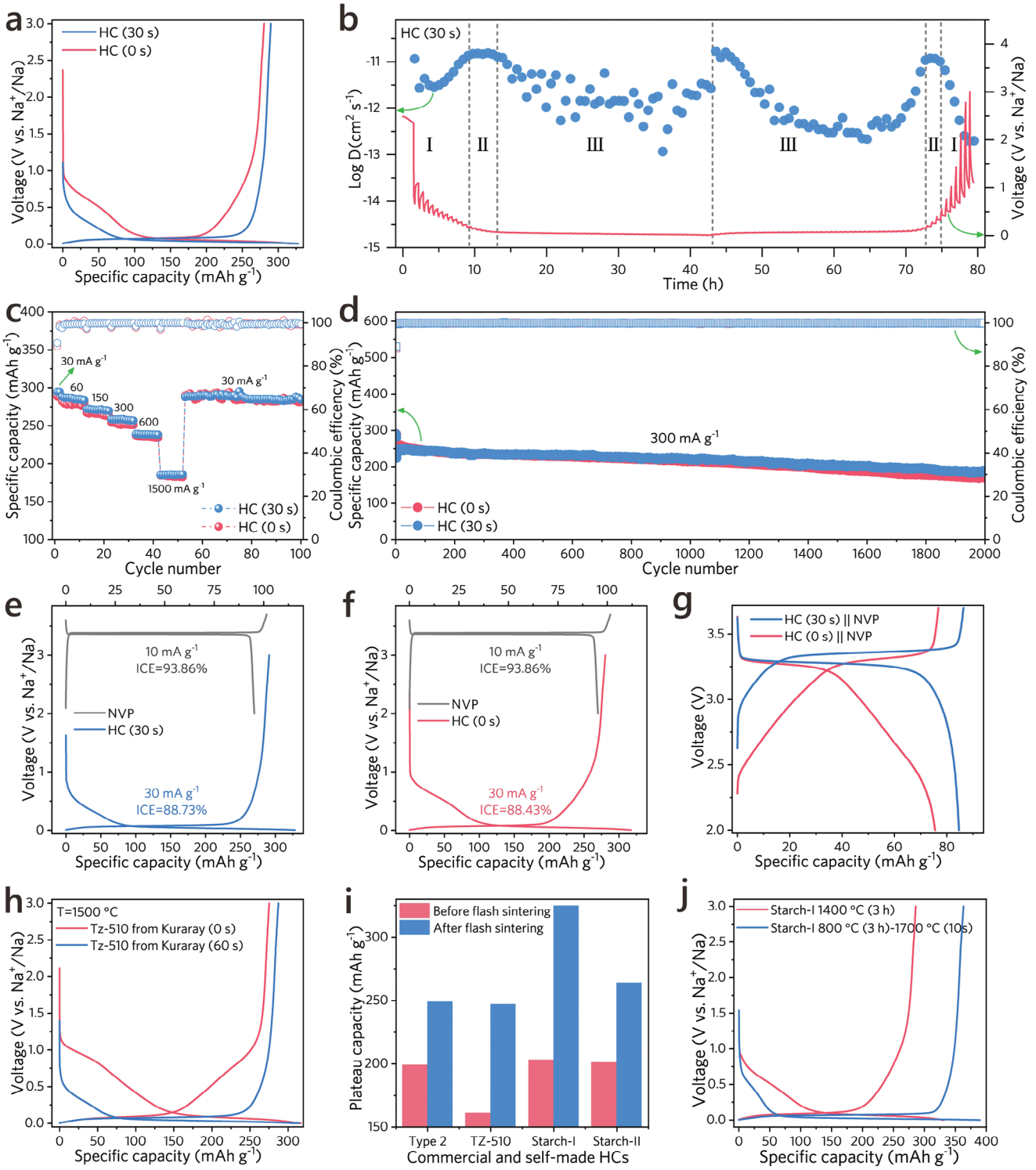

Figure 6. High-plateau-capacity HCs enable better Na-ion batteries and strategy universality. a) First-cycle discharge/charge profiles of HC (0 s) and HC (30 s) electrodes. b) GITT curve and corresponding Na^+ diffusion coefficient curves of the HC (30 s) anode during the first discharge/charge processes. c) Rate performance of HC (0 s) and HC (30 s) electrodes at various current densities of 30, 60, 150, 300, 600, and 1500 mA g^{-1} and long-term cycling stability at 30 mA g^{-1}. d) Ultra-long cycling test of HC (0 s) and HC (30 s) electrodes at 300 mA g^{-1}. e) The theoretical matching graph of charge and discharge curves for the NVP cathode and HC (30 s) anode. f) The theoretical matching graph of charge and discharge curves for the NVP cathode and HC (0 s) anode. g) Comparison of the charge/discharge profiles of HC (30 s) || NVP and HC (0 s) || NVP full cells at 10 mA g^{-1}. h) First-cycle discharge/charge profiles of Tz-510 HCs from Kuraray Corporation before and after flash sintering at 1500 °C for 60 s. i) The bar graph of the plateau capacity of Type 2 and TZ-510 from Kuraray Corporation and home-made starch-I and starch-II HCs before and after flash sintering treatment. j) First-cycle discharge/charge profiles of home-made starch-I HC (1400 °C, 3 h) and starch-I HC (800 °C, 3 h and 1700 °C, 10 s), respectively.

discharge and charge capacities of 327.9 and 289.8 mAh g^{-1}, respectively. Notably, the HC (30 s) anode presents a comparable first-cycle Coulombic efficiency (88.38%) to the pristine HC, indicating that the thermal pulse treatment does not cause irreversible side reactions while boosting the total and plateau capacities. Cyclic voltammetry (CV) curves of HC (0 s) and HC (30 s) anodes are compared in Figures S32 and S33 (Supporting Information) at various scan rates from 0.1 to 10 mV s^{-1}. The drastic suppression of the reduction and oxidation peaks at around 0.6 V further reveals a significant decrease in the adsorption/desorption capacity of Na^+ ions in the slope region,[66] which is also consistent with the results of the differential capacitance (dQ/dV) curves (Figure S34, Supporting Information). Galvanostatic intermittent titration technique (GITT) can measure the ionic diffusion coefficient of HC anodes during the discharge/charge processes,[66] and divide the reaction into different stages according to the evolutionary trend. As shown in Figure 6b and Figure S35 (Supporting Information), the measured ionic diffusion coefficient curves show three distinct intervals, with intervals II and III corresponding to the slope region and plateau region, respectively. Apparently, the pristine HC anode presents a wide II region and a narrow III region. In stark contrast, the HC (30 s) anode shows a very narrow II region and an extended III regions, strongly demonstrating the transition from the slope region to the plateau region.

To gain insight into the impact of transient high-temperature treatment on the rate capability and cycling performance, half coin-cells with HC (0 s) and HC (30 s) as the working electrodes were activated at 30 mA g^{-1} for two cycles, and then ran for 10 cycles at 60, 150, 300, 600, and 1500 mA g^{-1}, respectively, and finally switched back to 30 mA g^{-1} for long-term stability test. As Figure 6c demonstrates, the HC (30 s) anode delivers higher reversible capacity at each current density, indicating that the appropriate local graphitization degree does not affect the transport and storage of Na^+ ions in HCs. Notably, the further improvement of graphitization degree will in turn lead to the decay in ionic transport and rate performance (e.g., HC (60 s) in Figure S36, Supporting Information). Application-oriented ultralong cycling test of pristine HC and HC (30 s) anodes were performed at 300 mA g^{-1} after two activation cycles at 30 mA g^{-1} (Figure 6d). The HC (30 s) anode shows comparable or even more stable cycling performance than the pristine HC (0 s) anode. More encouragingly, the HC (30 s) anode preserves a reversible capacity of 187 mAh g^{-1} and a capacity retention rate of 83.5% after 2000 cycles, demonstrating excellent application prospects. Moreover, the HC (30 s) anode still exhibits a plateau capacity advantage of over 40 mAh g^{-1} relative to the pristine HC electrode after 2000 cycles (Figure S37, Supporting Information). Given the above, our modulation and enhancement of the plateau capacity contribute to improving the comprehensive electrochemical performance of HCs to a large extent.

As an empirical proof, we used $Na_3V_2(PO_4)_3$ (NVP) cathode materials coupling the HC (30 s) and pristine HC (0 s) anodes to predict their full-cell performance (Figure 6e,f). Apparently, the HC (30 s) || NVP full cell shows higher specific capacity and significantly larger integral area associated with energy density than that of the pristine HC (0 s) || NVP full cell owing to the longer plateau region. In practice, our assembled HC (30 s) || NVP and HC (0 s) || NVP full cells exhibit reversible capacities of 84.6 and 75.5 mAh g^{-1} at 10 mA g^{-1}, respectively (Figure 6g; Figure S38, Supporting Information). More importantly, the HC (30 s) || NVP cell shows a significantly elongated and higher operating voltage plateaus during both discharge/charge processes. As such, the output energy density of HC (30 s) || NVP cell (198 Wh kg^{-1}) exceeds that of HC (0 s) || NVP cell (164 Wh kg^{-1}) by up to 20.7%. The optimal HC (30 s) anode also promotes the working plateau and energy density of $NaNi_xFe_yMn_{(1-x-y)}O_2$ (NFM) cathode-based full cell. As shown in Figures S38 and S39 (Supporting Information), the HC (30 s) || NFM and HC (0 s) || NFM cells show reversible capacities of 83.8 and 78.5 mAh g^{-1}, respectively. Clearly, the HC (30 s) || NFM cell can reach the plateau region more quickly and present minimal slope capacity during discharge. As expected, the HC (30 s) || NFM cell exhibits an energy density (171 Wh kg^{-1}) that is 18.8% higher than HC (0 s) || NFM cell (144 Wh kg^{-1}). To more accurately assess the improvement in energy density, pouch cells were assembled for comparison. The corresponding schematic diagram and charge-discharge curves are provided in Figure S40 (Supporting Information). The HC (30 s) || NVP pouch cell exhibited an energy density of 189.33 Wh kg^{-1}, representing an 18.44% increase compared to the 159.85 Wh kg^{-1} of the HC (0 s) || NVP cell.

2.5. The Universality of Carbon Phase Modulation Strategy on Commercial and Self-Made HCs

The precise carbon phase modulation strategy was further extended to various commercial hard carbons to illustrate the universal applicability of the method. As manifested in Figure 6h and Figures S41 and S42 (Supporting Information), both hard carbons (TZ-510 and Type 2) from Kuraray Corporation showed a significant decrease in the slope capacity after screening the optimal thermal pulse widths, while the plateau capacity was greatly improved. As demonstrated in Figure 6i, the plateau capacities of the Type 2 and TZ-510 anodes increase from 199 and 161 to 249 and 248 mAh g^{-1}, respectively, with growth rates of 25.13% and 54.04%. Moreover, XRD and Raman spectra of Type 2 and TZ-510 HCs before and after thermal pulse treatment show the consistent evolution laws that we found in Figure 2, strongly illustrating the generalizability of our method (Figures S41 and S42, Supporting Information).

In addition to commercial HCs, we have also independently synthesized HC materials starting from starch precursors. Specifically, two precursors were adopted: low-temperature (800 °C) pre-calcination combined with thermal pulse treatment of porous starch (1700 °C, starch-I, Figure 6j) and esterified starch (1468 °C, starch- II, Figure S43, Supporting Information). Clearly, the HCs synthesized by incorporating the thermal pulse step all deliver higher reversible and plateau capacities. Especially for Starch-I, it exhibits a reversible capacity of 363.2 mAh g^{-1} and a plateau capacity up to 325 mAh g^{-1}, which is currently the state-of-the-art level in the whole-plateau hard carbon research. As Figure 6i demonstrates, the plateau capacities of the starch-II anodes also increase from 202 to 266 mAh g^{-1}, respectively, concurrently achieving high initial Coulombic efficiencies of 93.17% and 87.21%. Given the above, our concept of modulating the localized graphitization degree and nanopore growth by thermal pulse treatment can be widely applied to various commercial and

self-made HCs, all of which can achieve precise control of working potentials and plateau capacities.

3. Conclusion

In summary, we have achieved accurate regulation of the local graphitization degree and closed pore growth of HCs within dozens of seconds, leading to kinetically controlled HCs with short-range ordered graphitic micro-domains and appropriately sized closed nanopores. More importantly, the optimized HC sample after flash sintering can yield a significantly prolonged and dominant low-voltage plateau below 0.1 V, with the optimal sample exhibiting a high plateau capacity of up to 325 mAh g^{-1}, just like graphite anodes in lithium-ion batteries. The pivotal role of high-plateau-capacity HC anodes in significantly boosting the energy density of SIB full batteries up to 20.7% has been convincingly demonstrated. Furthermore, this carbon phase regulation technology has been further extended to various commercial and independently synthesized HCs, demonstrating its robust universality. We have experimentally and theoretically elucidated the structural evolution of carbon phases and closed nanopores under pulses of different widths, as well as their correlation with Na^+ storage electrochemistry. This work paves the way for designing and synthesizing transformative HCs with customizable sodium storage mechanisms and their application in high-energy-density SIBs.

4. Experimental Section

Materials Synthesis: All the reagents are directly used without further treatment. Hard Carbon-B (BTR New Materials Group Co. Ltd.), Tz-510 (Kuraray), and Type 2 (Kuraray) are commercial HCs purchased directly from the company. The home-made HCs, starch-I and II, were synthesized by rice starch (Shanghai Yuanye Bio-Technology Co., Ltd). Specifically, the starch precursor was heated at a rate of 5 °C min^{-1} to 800 °C under an argon atmosphere and maintained for 3 h, resulting in Starch (800 °C). Further, Starch (800 °C) was heated to 1400 °C at a rate of 5 °C min^{-1} under an argon atmosphere and maintained for 3 h, yielding Starch (1400 °C). The flash sintering was performed in a self-built Joule heating setup equipped with a temperature control system and circulating cooling system. The above HCs (0.5–5 g) were enveloped in the cavity of carbon felt (2.5×8.5 cm) before flash sintering, with two sides of the carbon felt connected to the positive and negative poles of the clamp. After sealing the reaction chamber, three vacuum operations were performed to remove the internal air for subsequent operations. The carbon phase regulation of the above-mentioned HCs was then achieved under different pulse temperatures and pulse widths. As a comparison, the extreme graphitization of HCs was obtained by calcinating the HC sample at 2800 °C using a graphitization furnace.

Electrode Preparation and Battery Assembly: The anode electrode was fabricated by mixing the HCs and carboxymethyl cellulose (CMC) binder in a mass ratio of 95:5, and then stirring several times by a planetary ball mill. Subsequently, the slurry was cast onto copper foil, and then dried at 120 °C for 6 h in a vacuum oven. The electrodes were cut into 12 mm discs with an average mass loading of ≈2 mg cm^{-2}. The half-cells were constructed using coin-type cells (CR 2032), wherein Na metal foil and glass fiber (Whatman GF/D) were severed as counter electrode and separator, respectively. Additionally, 1 M $NaPF_6$ dissolved in dimethyl ether (DME) was adopted as an electrolyte. All the batteries were assembled in a glove box (MIKROUNA) with an oxygen and water content of less than 0.1 ppm. For preparing cathode electrode, the active material ($NaNi_xFe_yMn_{(1-x-y)}O_2$ (NFM) and $Na_3V_2(PO_4)_3$ (NVP)), conductive agent (super P) and polyvinylidene fluoride (PVDF) were mixed in N-methyl-2-pyrollidone solvent with a mass ratio of 8:1:1. The obtained mixture was stirred using a planetary ball mill, then coated onto a carbon-coated aluminum foil. After vacuum drying, the electrodes were cut into 12 mm discs with an average mass loading of 6 mg cm^{-2}. Full cells were assembled using coin-type cells (CR-2032), wherein HCs and NVP (or NFM) served as the anode and cathode, respectively, with the N/P ratio controlled within the range of 1.05 to 1.15. The electrolyte, consisting of 1 M $NaClO_4$ dissolved in a mixed solvent of EC: PC (v/v, 1:1), was employed to assemble the NFM || HC full cells. In contrast, NVP || HC full cells were constructed using an electrolyte of 1 M $NaPF_6$ dissolved in diglyme solvent.

Training Details for Machine Learning Interatomic Potential: The DeePMD-Kit package utilizes the smoothing method during the training process of the Deep Potential (DP) model.[67] For this work, the descriptor "se_e2_a" was used, which is short for the Deep Potential Smooth Edition (DeepPot-SE) constructed from all information (both angular and radial) of atomic configurations. The cutoff radius of adjacent atoms in the model was set to 6.0 Å, and the inverse distance was gradually smoothed from 0.5 Å to 6 Å. The filtering neural network was composed of three hidden layers[20, 40, 80], while the fitting network consisted of [240, 240, 240]. The neural network was initialized with random parameters, and the total number of training steps was 600 000. The Adam stochastic gradient descent method was used for training the model,[68] which caused the learning rate to exponentially decrease relative to the starting value of 0.001. The decay step and decay rate were set to 2000 and 0.996, respectively.

The loss function L was defined as follows:

$$L\left(p_e, p_f, p_\xi\right) = \frac{p_e}{N}\Delta E^2 + \frac{p_f}{3N}\sum_i \left|\Delta F_i\right|^2 + \frac{p_\xi}{9N}\|\Delta\Xi\|^2 \quad (1)$$

where ΔE and ΔF_i represent the mean square errors in energies and forces, respectively. The energy perfector p_e decreased from 0.02 to 1, while the force prefactor p_f decreased from 1000 to 1. It is worth noting that the training process did not include virial data.

Materials Characterization and Electrochemical Measurements: The characterization of material structure and morphology, as well as electrochemical measurements, are provided in the experimental section of the supporting materials.

Supporting Information

Supporting Information is available from the Wiley Online Library or from the author.

Acknowledgements

This work was supported by the National Natural Science Foundation of China (Grant Nos. 92372101, 52122211, 22301106, and 21875155), the Fundamental Research Funds for the Central Universities (20720220010), the National Key Research and Development Program of China (2021YFA1201502). L. Zhang acknowledges the support of the Nanqiang Young Top-notch Talent Fellowship at Xiamen University. S.R. Fang and T.F. Wu from the Information and Network Center of Xiamen University are acknowledged for their help with the Graphics Processing Unit (GPU) computing. The authors also thank Prof. Yongsheng Hu in the Institute of Physics, Chinese Academy of Sciences for his helpful guidance.

Conflict of Interest

The authors declare no conflict of interest.

Author Contributions

J.J.L., Y.W.Y., and L.H. contributed equally to this work. L.Z. and S.W. designed and supervised this work. J.L., L.H., L.S., M.L., and X.Z. carried out

the synthesis and the electrochemical experiments. J.L., Q.Z.Z., Z.S., K.F., and Y.H. performed ex situ/in situ XRD, FT-IR, Raman, SEM, and TEM characterizations. Y.Y. and S.W. carried out DFT, AIMD, and DeepMD calculations. J.L., Y.Y., and L.Z. wrote the manuscript. L.Z., S.W., and J.Z. appraised and revised the paper. Y.C. and Q.B.Z. participated in the analysis of experimental data and the discussion of results, as well as the preparation of the manuscript.

Data Availability Statement

The data that support the findings of this study are available from the corresponding author upon reasonable request.

Keywords

low-voltage discharge/charge plateaus, metastable hard carbon, Na-ion battery, transient high-temperature pulse, tunable local carbon phases

Received: May 23, 2024
Revised: August 6, 2024
Published online:

[1] W. Yan, Z. Mu, Z. Wang, Y. Huang, D. Wu, P. Lu, J. Lu, J. Xu, Y. Wu, T. Ma, M. Yang, X. Zhu, Y. Xia, S. Shi, L. Chen, H. Li, F. Wu, *Nat. Energy* **2023**, *8*, 800.
[2] J. Y. Hwang, S. T. Myung, Y. K. Sun, *Chem. Soc. Rev.* **2017**, *46*, 3529.
[3] C. Vaalma, D. Buchholz, M. Weil, S. Passerini, *Nat. Rev. Mater.* **2018**, *3*, 18013.
[4] Y. Li, Q. Zhou, S. Weng, F. Ding, X. Qi, J. Lu, Y. Li, X. Zhang, X. Rong, Y. Lu, X. Wang, R. Xiao, H. Li, X. Huang, L. Chen, Y.-S. Hu, *Nat. Energy* **2022**, *7*, 511.
[5] A. Rudola, R. Sayers, C. J. Wright, J. Barker, *Nat. Energy* **2023**, *8*, 215.
[6] X. Wang, Q. Zhang, C. Zhao, H. Li, B. Zhang, G. Zeng, Y. Tang, Z. Huang, I. Hwang, H. Zhang, S. Zhou, Y. Qiu, Y. Xiao, J. Cabana, C.-J. Sun, K. Amine, Y. Sun, Q. Wang, G.-L. Xu, L. Gu, Y. Qiao, S.-G. Sun, *Nat. Energy* **2024**, *9*, 184.
[7] C. Zhao, Q. Wang, Z. Yao, J. Wang, B. Sánchez-Lengeling, F. Ding, X. Qi, Y. Lu, X. Bai, B. Li, H. Li, A. Aspuru-Guzik, X. Huang, C. Delmas, M. Wagemaker, L. Chen, Y.-S. Hu, *Science* **2020**, *370*, 708.
[8] T. Bashir, S. Zhou, S. Yang, S. A. Ismail, T. Ali, H. Wang, J. Zhao, L. Gao, *Electrochem. Energy Rev.* **2023**, *6*, 5.
[9] M. Lee, J. Hong, J. Lopez, Y. Sun, D. Feng, K. Lim, W. C. Chueh, M. F. Toney, Y. Cui, Z. Bao, *Nat. Energy* **2017**, *2*, 861.
[10] K. Sada, J. Darga, A. Manthiram, *Adv. Energy Mater.* **2023**, *13*, 2302321.
[11] C. Chen, Y. Wen, X. Hu, X. Ji, M. Yan, L. Mai, P. Hu, B. Shan, Y. Huang, *Nat. Commun.* **2015**, *6*, 6929.
[12] Y. Jin, P. M. L. Le, P. Gao, Y. Xu, B. Xiao, M. H. Engelhard, X. Cao, T. D. Vo, J. Hu, L. Zhong, B. E. Matthews, R. Yi, C. Wang, X. Li, J. Liu, J.-G. Zhang, *Nat. Energy* **2022**, *7*, 718.
[13] S. Wang, L. Wang, Z. Zhu, Z. Hu, Q. Zhao, J. Chen, *Angew. Chem., Int. Ed.* **2014**, *53*, 5892.
[14] Z. Tian, Y. Zhang, J. Zhu, Q. Li, T. Liu, M. Antonietti, *Adv. Energy Mater.* **2021**, *11*, 2102489.
[15] B. Xiao, T. Rojo, X. Li, *ChemSusChem* **2019**, *12*, 133.
[16] D. A. Stevens, J. R. Dahn, *J. Electrochem. Soc.* **2000**, *147*, 1271.
[17] Y. Li, Y. Lu, P. Adelhelm, M. M. Titirici, Y. S. Hu, *Chem. Soc. Rev.* **2019**, *48*, 4655.
[18] X. Dou, I. Hasa, D. Saurel, C. Vaalma, L. Wu, D. Buchholz, D. Bresser, S. Komaba, S. Passerini, *Mater. Today* **2019**, *23*, 87.
[19] D. Saurel, B. Orayech, B. Xiao, D. Carriazo, X. Li, T. Rojo, *Adv. Energy Mater.* **2018**, *8*, 1703268.
[20] Y. Chu, J. Zhang, Y. Zhang, Q. Li, Y. Jia, X. Dong, J. Xiao, Y. Tao, Q. H. Yang, *Adv. Mater.* **2023**, *35*, 2212186.
[21] S. Alvin, H. S. Cahyadi, J. Hwang, W. Chang, S. K. Kwak, J. Kim, *Adv. Energy Mater.* **2020**, *10*, 2000283.
[22] H. Au, H. Alptekin, A. C. S. Jensen, E. Olsson, C. A. O'Keefe, T. Smith, M. Crespo-Ribadeneyra, T. F. Headen, C. P. Grey, Q. Cai, A. J. Drew, M.-M. Titirici, *Energy Environ. Sci.* **2020**, *13*, 3469.
[23] D. Chen, W. Zhang, K. Luo, Y. Song, Y. Zhong, Y. Liu, G. Wang, B. Zhong, Z. Wu, X. Guo, *Energy Environ. Sci.* **2021**, *14*, 2244.
[24] S. Qiu, L. Xiao, M. L. Sushko, K. S. Han, Y. Shao, M. Yan, X. Liang, L. Mai, J. Feng, Y. Cao, X. Ai, H. Yang, J. Liu, *Adv. Energy Mater.* **2017**, *7*, 1700403.
[25] Y. Li, A. Vasileiadis, Q. Zhou, Y. Lu, Q. Meng, Y. Li, P. Ombrini, J. Zhao, Z. Chen, Y. Niu, X. Qi, F. Xie, R. van der Jagt, S. Ganapathy, M.-M. Titirici, H. Li, L. Chen, M. Wagemaker, Y.-S. Hu, *Nat. Energy* **2024**, *9*, 134.
[26] H. Kim, J. C. Hyun, D. H. Kim, J. H. Kwak, J. B. Lee, J. H. Moon, J. Choi, H. D. Lim, S. J. Yang, H. M. Jin, D. J. Ahn, K. Kang, H. J. Jin, H. K. Lim, Y. S. Yun, *Adv. Mater.* **2023**, *35*, 2209128.
[27] Z. Li, C. Bommier, Z. S. Chong, Z. Jian, T. W. Surta, X. Wang, Z. Xing, J. C. Neuefeind, W. F. Stickle, M. Dolgos, P. A. Greaney, X. Ji, *Adv. Energy Mater.* **2017**, *7*, 1602894.
[28] W. Li, X. Guo, K. Song, J. Chen, J. Zhang, G. Tang, C. Liu, W. Chen, C. Shen, *Adv. Energy Mater.* **2023**, *13*, 2300648.
[29] Z. Wang, X. Feng, Y. Bai, H. Yang, R. Dong, X. Wang, H. Xu, Q. Wang, H. Li, H. Gao, C. Wu, *Adv. Energy Mater.* **2021**, *11*, 2003854.
[30] H. He, J. He, H. Yu, L. Zeng, D. Luo, C. Zhang, *Adv. Energy Mater.* **2023**, *13*, 2300357.
[31] Z. Zheng, S. Hu, W. Yin, J. Peng, R. Wang, J. Jin, B. He, Y. Gong, H. Wang, H. J. Fan, *Adv. Energy Mater.* **2023**, *14*, 2303064.
[32] Y. Youn, B. Gao, A. Kamiyama, K. Kubota, S. Komaba, Y. Tateyama, *NPJ Comput.Mater.* **2021**, *7*, 48.
[33] N. Sun, J. Qiu, B. Xu, *Adv. Energy Mater.* **2022**, *12*, 2200715.
[34] L. F. Zhao, Z. Hu, W. H. Lai, Y. Tao, J. Peng, Z. C. Miao, Y. X. Wang, S. L. Chou, H. K. Liu, S. X. Dou, *Adv. Energy Mater.* **2020**, *11*, 2002704.
[35] X. Feng, Y. Li, Y. Li, M. Liu, L. Zheng, Y. Gong, R. Zhang, F. Wu, C. Wu, Y. Bai, *Energy Environ. Sci.* **2024**, *17*, 1387.
[36] B. Zhang, M. Deschamps, M. R. Ammar, E. Raymundo-Piñero, L. Hennet, D. Batuk, J. M. Tarascon, *Adv. Mater. Technol.* **2016**, *2*, 1600227.
[37] B. Zhang, C. M. Ghimbeu, C. Laberty, C. Vix-Guterl, J. M. Tarascon, *Adv. Energy Mater.* **2015**, *6*, 1501588.
[38] Z. Tang, S. Zhou, Y. Huang, H. Wang, R. Zhang, Q. Wang, D. Sun, Y. Tang, H. Wang, *Electrochem. Energy Rev.* **2023**, *6*, 8.
[39] N. LeGe, X.-X. He, Y.-X. Wang, Y. Lei, Y.-X. Yang, J.-T. Xu, M. Liu, X. Wu, W.-H. Lai, S.-L. Chou, *Energy Environ. Sci.* **2023**, *16*, 5688.
[40] Z. Lu, J. Wang, W. Feng, X. Yin, X. Feng, S. Zhao, C. Li, R. Wang, Q. A. Huang, Y. Zhao, *Adv. Mater.* **2023**, *35*, 2211461.
[41] Z. Guo, Z. Xu, F. Xie, J. Jiang, K. Zheng, S. Alabidun, M. Crespo-Ribadeneyra, Y. S. Hu, H. Au, M. M. Titirici, *Adv. Mater.* **2023**, *35*, 2304091.
[42] L. Kitsu Iglesias, E. N. Antonio, T. D. Martinez, L. Zhang, Z. Zhuo, S. J. Weigand, J. Guo, M. F. Toney, *Adv. Energy Mater.* **2023**, *13*, 2302171.
[43] Q. Li, J. Zhang, L. Zhong, F. Geng, Y. Tao, C. Geng, S. Li, B. Hu, Q. H. Yang, *Adv. Energy Mater.* **2022**, *12*, 2201734.
[44] J. M. Stratford, A. K. Kleppe, D. S. Keeble, P. A. Chater, S. S. Meysami, C. J. Wright, J. Barker, M. M. Titirici, P. K. Allan, C. P. Grey, *J. Am. Chem. Soc.* **2021**, *143*, 14274.
[45] A. Kamiyama, K. Kubota, D. Igarashi, Y. Youn, Y. Tateyama, H. Ando, K. Gotoh, S. Komaba, *Angew. Chem., Int. Ed.* **2021**, *60*, 5114.
[46] S. Komaba, *Chem. Lett.* **2020**, *49*, 1507.
[47] C. Zhao, Q. Wang, Y. Lu, B. Li, L. Chen, Y. S. Hu, *Sci. Bull.* **2018**, *63*, 1125.
[48] T. Xu, X. Qiu, X. Zhang, Y. Xia, *Chem. Eng. J.* **2023**, *452*, 139514.

[49] Z. Tang, R. Zhang, H. Wang, S. Zhou, Z. Pan, Y. Huang, D. Sun, Y. Tang, X. Ji, K. Amine, M. Shao, *Nat. Commun.* **2023**, *14*, 6024.
[50] X. X. He, W. H. Lai, Y. Liang, J. H. Zhao, Z. Yang, J. Peng, X. H. Liu, Y. X. Wang, Y. Qiao, L. Li, X. Wu, S. L. Chou, *Adv. Mater.* **2023**, *35*, 2302613.
[51] D. X. Luong, K. V. Bets, W. A. Algozeeb, M. G. Stanford, C. Kittrell, W. Chen, R. V. Salvatierra, M. Ren, E. A. McHugh, P. A. Advincula, Z. Wang, M. Bhatt, H. Guo, V. Mancevski, R. Shahsavari, B. I. Yakobson, J. M. Tour, *Nature* **2020**, *577*, 647.
[52] Q. Dong, Y. Yao, S. Cheng, K. Alexopoulos, J. Gao, S. Srinivas, Y. Wang, Y. Pei, C. Zheng, A. H. Brozena, H. Zhao, X. Wang, H. E. Toraman, B. Yang, I. G. Kevrekidis, Y. Ju, D. G. Vlachos, D. Liu, L. Hu, *Nature* **2022**, *605*, 470.
[53] M. G. Stanford, K. V. Bets, D. X. Luong, P. A. Advincula, W. Chen, J. T. Li, Z. Wang, E. A. McHugh, W. A. Algozeeb, B. I. Yakobson, J. M. Tour, *ACS Nano* **2020**, *14*, 13691.
[54] Y. Chen, G. C. Egan, J. Wan, S. Zhu, R. J. Jacob, W. Zhou, J. Dai, Y. Wang, V. A. Danner, Y. Yao, K. Fu, Y. Wang, W. Bao, T. Li, M. R. Zachariah, L. Hu, *Nat. Commun.* **2016**, *7*, 12332.
[55] X. Chen, N. Sawut, K. Chen, H. Li, J. Zhang, Z. Wang, M. Yang, G. Tang, X. Ai, H. Yang, Y. Fang, Y. Cao, *Energy Environ. Sci.* **2023**, *16*, 4041.
[56] Z. Hong, Y. Zhen, Y. Ruan, M. Kang, K. Zhou, J. M. Zhang, Z. Huang, M. Wei, *Adv. Mater.* **2018**, *30*, 1802035.
[57] D. Igarashi, Y. Tanaka, K. Kubota, R. Tatara, H. Maejima, T. Hosaka, S. Komaba, *Adv. Energy Mater.* **2023**, *13*, 2302647.
[58] Y. Huang, X. Zhong, X. Hu, Y. Li, K. Wang, H. Tu, W. Deng, G. Zou, H. Hou, X. Ji, *Adv. Funct. Mater.* **2024**, *34*, 2308392.
[59] Y. Morikawa, S. Nishimura, R. Hashimoto, M. Ohnuma, A. Yamada, *Adv. Energy Mater.* **2019**, *10*, 1903176.
[60] Z. Yu, C. Chen, Q. Liu, J. Liu, M. Tang, Y. Zhu, B. Zhang, *Energy Storage Mater.* **2023**, *60*, 102805.
[61] D. Saurel, J. Segalini, M. Jauregui, A. Pendashteh, B. Daffos, P. Simon, M. Casas-Cabanas, *Energy Storage Mater.* **2019**, *21*, 162.
[62] J. Yang, X. Wang, W. Dai, X. Lian, X. Cui, W. Zhang, K. Zhang, M. Lin, R. Zou, K. P. Loh, Q. H. Yang, W. Chen, *Nanomicro. Lett.* **2021**, *13*, 98.
[63] Q. Li, X. Liu, Y. Tao, J. Huang, J. Zhang, C. Yang, Y. Zhang, S. Zhang, Y. Jia, Q. Lin, Y. Xiang, J. Cheng, W. Lv, F. Kang, Y. Yang, Q. H. Yang, *Natl. Sci. Rev.* **2022**, *9*, nwac084.
[64] M. Song, Z. Yi, R. Xu, J. Chen, J. Cheng, Z. Wang, Q. Liu, Q. Guo, L. Xie, C. Chen, *Energy Storage Mater.* **2022**, *51*, 620.
[65] H. Moriwake, A. Kuwabara, C. A. J. Fisher, Y. Ikuhara, *RSC Adv.* **2017**, *7*, 36550.
[66] J. L. Xia, D. Yan, L. P. Guo, X. L. Dong, W. C. Li, A. H. Lu, *Adv. Mater.* **2020**, *32*, 2000447.
[67] L. Zhang, J. Han, H. Wang, R. Car, W. E., *Phys. Rev. Lett.* **2018**, *120*, 143001.
[68] D. P. Kingma, J. Ba, arXiv preprint **2017**, 1412.6980v9.